



1 **Spatiotemporal dynamics and drivers of bare soil albedo in European** 2 **croplands**

3 Ke Yu¹, Yang Su^{1,2,3,*}, Philippe Ciais¹, Ronny Lauerwald^{2,4}, David Makowski⁵, Tianqi Shi¹, Shengbiao
4 Wu⁶, Petra Sieber⁷, Chuanlong Zhou¹, Daniel S. Goll¹

5
6 ¹Laboratoire des Sciences du Climat et de l'Environnement, LSCE/IPSL, CEA-CNRS-UVSQ, Université Paris-Saclay, 91191
7 Gif-sur-Yvette, France.

8 ²UMR ECOSYS, INRAE AgroParisTech, Université Paris-Saclay, 91120 Palaiseau, France

9 ³Département d'Informatique, École Normale Supérieure - PSL, 75005 Paris, France

10 ⁴Department Geoscience, Environment & Society-BGEOSYS, Université Libre de Bruxelles, Bruxelles, Belgium

11 ⁵UMR MIA PS, INRAE AgroParisTech, Université Paris-Saclay, 91120 Palaiseau, France

12 ⁶Future Urbanity & Sustainable Environment (FUSE) Lab, Division of Landscape Architecture, Department of Architecture,
13 Faculty of Architecture, The University of Hong Kong, Pokfulam, Hong Kong Special Administrative Region, China

14 ⁷Institute for Atmospheric and Climate Science, ETH Zurich, Zurich, Switzerland

15
16 *Correspondence to:* Yang Su (yang.su@ens.fr)

17
18 **Abstract.** Bare soil albedo plays a critical role in regulating surface energy balance and land-atmosphere interactions in
19 agricultural systems, yet its spatiotemporal variability and controlling factors remain poorly quantified at the field scale across
20 heterogeneous cropland landscapes. To address this, we investigate the spatial patterns and temporal dynamics of bare soil
21 albedo in European croplands. We develop a method to reconstruct field-scale, spatiotemporally continuous bare soil albedo
22 at a 5-day temporal resolution and 0.3 km spatial resolution using Sentinel-2 reflectance observations. Bare soil periods are
23 identified by multiple spectral indices and the corresponding soil albedo values are derived for the period 2018-2020 using a
24 novel machine learning framework. Two random forest models were employed to separately capture the long-term spatial
25 structure and short-term temporal anomalies of bare soil albedo, allowing gaps caused by clouds, snow, and vegetation cover
26 to be bridged. Model evaluation against independent site observations and existing products shows that the estimated bare soil
27 albedo reproduces observed spatial gradients and seasonal variability across European croplands. Such variations in bare soil
28 albedo are jointly controlled by soil properties, observation geometry and short-term soil moisture dynamics rather than by
29 any single factor. Because these variations are of the same order of magnitude as radiation management solutions, soil radiative
30 properties must be considered in their assessment. The resulting bare soil albedo offers a process-oriented basis for improving
31 the representation of surface radiative properties and land-atmosphere coupling in agroecosystem and land surface models.



32 **1 Introduction**

33 Albedo, the proportion of incoming solar radiation reflected by a surface, modulates the local and global heat budgets by
34 controlling the amount of incoming solar radiation that is absorbed and transformed into heat. Given that croplands occupy
35 37% of the Earth's land area (FAO 2023), it is important to quantify the albedo-related climate impacts of agricultural practices
36 (Davin et al., 2014; Sieber et al., 2022) as they can offset or enhance the effects of greenhouse gas emissions (Bright et al.,
37 2015).

38 In agricultural areas, the soil is bare (i.e., without any plant or litter cover) between successive growing periods, typically
39 during a few months between the harvest of one crop and the sowing of the next crops. Bare soil albedo affects crop growth
40 by modulating the local surface energy balance (e.g., through soil temperature and soil moisture) (Bsaibes et al., 2009; Zhang
41 et al., 2022). It also influences the magnitude of agriculture-induced albedo changes and the resulting climate impacts (i.e.,
42 radiative forcing). Bare soil albedo is controlled by a combination of intrinsic soil properties including texture, mineral
43 composition, roughness, organic matter content, and bulk density, as well as dynamic factors such as soil moisture and solar
44 illumination geometry (Hapke, 1981; Matthias et al., 2000; Cierniewski et al., 2018; He et al., 2019). The interaction of these
45 factors, as well as the frequent agricultural activities (e.g., harvest, changes of crop types), gives rise to pronounced spatial
46 heterogeneity and rapid temporal variability, particularly in intensively managed agricultural landscapes (Starr et al., 2020;
47 Sieber et al., 2022). Nevertheless, the spatiotemporal variability and controlling mechanisms of bare soil albedo remain
48 insufficiently quantified at field scale across heterogeneous cropland regions.

49 Ground-based measurements, airborne or unmanned aerial vehicle measurements measure incoming and outgoing solar
50 radiation over the soil surface, but have limited spatial coverage (Canisius et al., 2019; Pastorello et al., 2020; Amazirh et al.,
51 2021, Pan et al., 2024). Satellites observations provide comprehensive spectral reflectance data with extensive temporal and
52 spatial coverage, allowing for the monitoring of bare soil albedo datasets at regional to global scale (Lesaignoux 2009;
53 Verheijen et al., 2013; Carrer et al., 2014; Cierniewski et al., 2017; Rizzo et al., 2023). However, commonly used satellite-
54 based products, such as those derived from MODIS, typically operate at spatial resolutions of several hundred meters to
55 kilometers and temporal resolutions of weeks to months, which limits their ability to resolve field-scale heterogeneity and
56 short-term albedo dynamics driven by soil moisture fluctuations and agricultural management (Zhou et al., 2005; Houldcroft
57 et al., 2009; Cheng et al., 2014; He et al., 2019).

58 For example, the ECOCLIMAP project provides bare soil albedo datasets at a coarse spatial resolution of 1 km and a temporal
59 resolution ranging from 10 days to monthly, which is designed for use in climate modelling, but does not meet the resolution
60 requirements for effective agricultural monitoring able to capture the impacts of agricultural management (Masson et al., 2003;
61 Faroux et al., 2013; Carrer et al., 2014). While products at sufficiently high spatiotemporal resolution exist but are limited to



62 small regions or short time periods, constraining their applicability for continental-scale process analysis (Bsaibes et al., 2009;
63 Roujean et al., 2018).

64 Numerical models based on physical processes such as radiative transfer models are also applied to produce bare soil albedo
65 combined with satellite-based reflectance (Jacquemoud et al., 1992; Babellet et al., 2018). For example, a global ~50 km monthly
66 bare soil albedo map was generated by radiative transfer equations from 2001 to 2009 based on MODIS surface albedo (Pinty
67 et al., 2011). However, this coarse spatiotemporal resolution limits its utility in evaluating albedo-related climate impacts of
68 land management. Additionally, because of issues related to calibration and validation, the reliability of the simulations
69 provided by process-based models is limited (Bsaibes et al., 2009).

70 Machine learning can investigate bare soil albedo dynamics by considering complex dependencies between variables and
71 deliver more accurate and reliable predictions than traditional statistical methods (Jones et al., 2017; Nguyen et al., 2021;
72 Buster et al., 2024). This capability is particularly valuable for understanding the complex interactions between bare soil albedo,
73 climate, and pedological features, as opposed to traditional statistical approaches that typically rely on simple relationships
74 between bare soil albedo and single features such as the exponential relationship between bare soil albedo and soil water
75 content (Lesaigroux et al., 2009; Gascoïn et al., 2009; Verheijen et al., 2013). Additionally, machine learning-based predictions
76 of bare soil albedo can address spatiotemporal gaps in satellite observations (Ren et al., 2022) caused by snow and cloud cover,
77 enabling large-scale continuous and dynamic analysis and simulation of bare soil albedo in crop regions under historical,
78 present and future scenarios. When combined with high-resolution satellite imagery (e.g., Sentinel-2 satellite with 0.01 km
79 spatial resolution), machine learning enables the reconstruction of continuous bare soil albedo at both large scales and high
80 resolution, especially in cropland regions.

81 In this study, we investigate the spatiotemporal variability and drivers of bare soil albedo across European croplands by
82 integrating Sentinel-2 observations with a machine-learning reconstruction framework. We test two hypotheses: (1) for the
83 spatial distribution of bare soil albedo, soil properties exert a stronger control than radiative factors, and (2) for temporal
84 variability of bare soil albedo, fluctuation in soil moisture is more influential than static soil properties. To address these
85 hypotheses, our objectives are to (1) quantify the spatial patterns of bare soil albedo at the field scale across Europe, (2)
86 characterize the temporal dynamics of bare soil albedo during bare soil periods, and (3) identify the relative contributions of
87 soil and topographic properties versus dynamic drivers such as soil moisture and solar geometry. By doing so, we provide a
88 process-oriented assessment of bare soil albedo variability that is relevant for understanding the energy balance of agricultural
89 systems and improving the representation of surface radiative properties in land surface models.

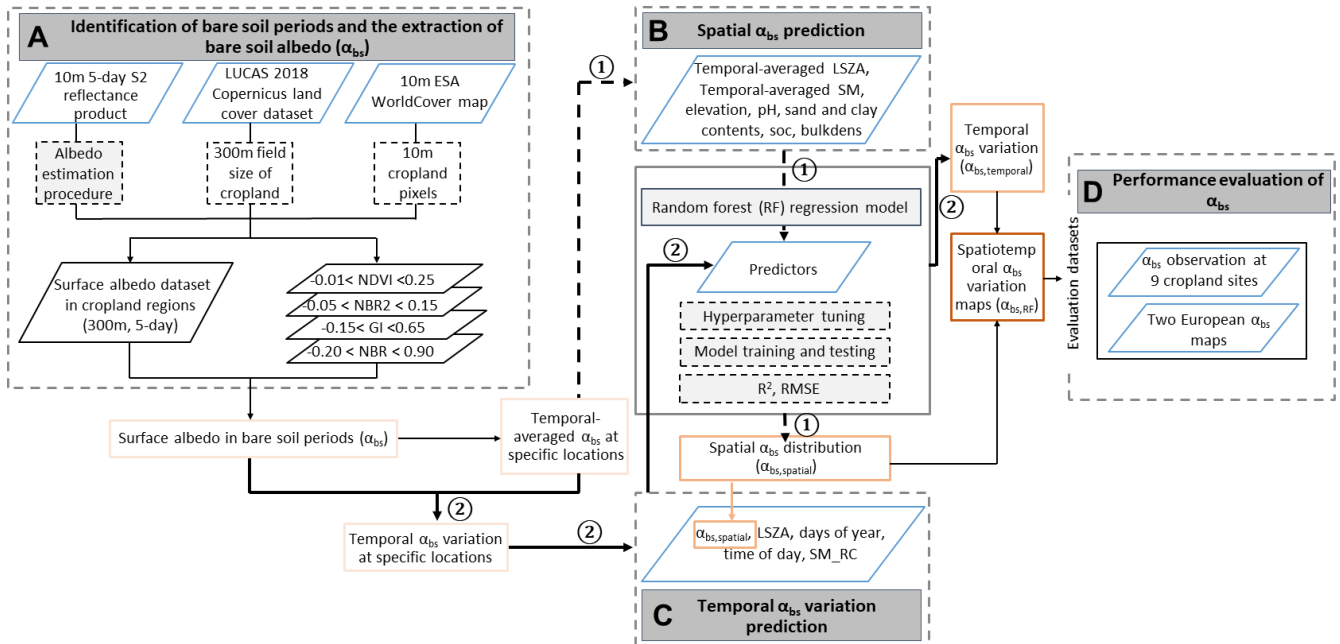
90 **2 Material and methods**

91 **2.1 Data source and processing**

92 Our approach consists of the following steps (Fig. 1): First, we identified bare soil periods and extracted corresponding bare
93 soil albedo (α_{bs}) values from Sentinel-2 surface albedo products based on thresholds of satellite-derived indices. Second, we
94 trained two random forest (RF) models on Sentinel-2 surface albedo during bare soil periods for the prediction of spatial



95 distribution and temporal anomaly of α_{bs} at the European cropland scale. Third, we compared the predicted α_{bs} to existing α_{bs}
 96 datasets at site or European scales.



97
 98 **Figure 1** The flow chart of the data processing procedure. ‘NDVI, NBR2, GI, NBR’ are the normalized difference vegetation
 99 index (NDVI), normalized burn ratio 2 index (NBR2), greenness index (GI) and the normalized burn ratio index (NBR),
 100 respectively. ‘LSZA, SM, SM_RC, SOC, bulkdens’ represent local solar zenith angle (LSZA), soil moisture (SM), relative
 101 SM anomaly (SM_RC), soil organic carbon (SOC) and bulk density (bulkdens), respectively. “ $\alpha_{bs,spatial}$ ”, “ $\alpha_{bs,temporal}$ ” and “ $\alpha_{bs,RF}$ ”
 102 are the spatial distribution and temporal variation of bare soil albedo (α_{bs}) predicted by random forest models, and the final
 103 spatiotemporal α_{bs} maps, respectively. R^2 and RMSE are the coefficient of determination and root mean square error. The bold
 104 black dotted (“①”) and solid arrow (“②”) lines represent the procedure of spatial and temporal α_{bs} prediction, respectively.

105 2.1.1 Daily surface albedo

106 We derived 5-day 0.3 km black-sky albedo (BSA) and white-sky albedo (WSA) from the 0.01 km Sentinel-2 surface
 107 reflectance product for the period 2018-2020 using the approach of Lin et al. (2023). This approach uses a look-up table trained
 108 on prior information on the angular-based relationships between surface reflectance and broadband albedo derived from the
 109 0.5 km resolution MODIS BRDF product (MCD43A1). The look-up table is used to derive BSA and WSA from Sentinel-2
 110 surface reflectance product assuming the same relationship as between BSA and WSA and MODIS BRDF product. The daily
 111 albedo derived from Sentinel-2 reflectance shows a higher correlation with site observations ($n=588$) ($R^2=0.44$, $RMSE=0.004$)
 112 compared to the MODIS product ($R^2=0.16$, $RMSE=0.06$) (Fig. S8). This provides support for the use of the Sentinel-2
 113 reflectance in combination with the look-up table trained on MODIS.



114 A cloud probability product was utilized to filter out images affected by cloud cover. This process employed cloud masking
115 parameters as outlined in the Google Earth Engine Sentinel-2 cloud masking tutorial ([https://developers.google.com/earth-](https://developers.google.com/earth-engine/tutorials/community/sentinel-2-s2cloudless)
116 [engine/tutorials/community/sentinel-2-s2cloudless](https://developers.google.com/earth-engine/tutorials/community/sentinel-2-s2cloudless)).
117 Specifically, the 'CLOUD FILTER' and the 'BUFFER' parameters were set to 10% and 0.02 km in this process. This framework
118 was accomplished on the Google Earth Engine platform to produce the datasets of BSA and WSA with a spatial resolution of
119 0.3 km at a European scale. We used 0.3 km as the spatial resolution to match the average field size in Europe and ensure a
120 sufficiently large number of data points required for machine learning (see below).
121 We finally obtained the 5-day shortwave surface albedo (α) from BSA and WSA weighted by the fraction of diffuse solar
122 radiation (k_d):

$$123 \quad \alpha = (1 - k_d) \times \text{BSA} + k_d \times \text{WSA} \quad (1)$$

124 The parameter k_d is computed based on the global surface solar radiation (S_0 , MJ m⁻² d⁻¹) and extra-terrestrial solar radiation
125 (S_e , MJ m⁻² d⁻¹) during the same periods with BSA and WSA datasets. Details of the diffuse solar radiation model can be found
126 in Yang (2019). S_0 corresponds to the daily average of hourly downward surface solar radiation at the spatial resolution of
127 ~11.1 km from the European Centre for Medium-Range Weather Forecasts (ECMWF) Reanalysis 5 (ERA5) (Hersbach et al.,
128 2020). S_e is estimated from the solar constant, the solar declination and the time of the year in a specific location, which is
129 described by Allen et al. (2006).

130 Filtering Sentinel-2 surface albedo during bare soil periods from 2018 to 2020 using spectral indices, we obtained 132,487 soil
131 samples in the European cropland regions. The average Sentinel-2 α_{bs} of all 0.3 km resolution bare soil pixels is approximately
132 0.18 ± 0.03 (mean \pm standard deviation). Details of extracting bare soil periods in European cropland regions and defining the
133 0.3 km spatial resolution of Sentinel-2 α_{bs} are described below.

134 We computed (1) the temporal average at each 0.3 km sample location for training and testing an RF model for the spatial
135 pattern of α_{bs} , and (2) the temporal anomaly of α_{bs} as the difference between the original α_{bs} and the temporal average. Samples
136 with an anomaly of 0 were removed as they represent locations with only a single α_{bs} observation, thus lacking temporal
137 representativeness. The α_{bs} anomaly dataset was used as the dependent feature for training and testing RF for the temporal
138 anomaly of α_{bs} .

139 **2.1.2 European cropland mask**

140 The ESA WorldCover product at 0.01 km spatial resolution generated from Sentinel-1 and Sentinel-2 observations in 2021
141 was utilized to identify croplands in Europe (<https://esa-worldcover.org/>) (Zanaga et al., 2022). This time-invariant product
142 includes 11 land cover types, including one class for croplands.

143 **2.1.3 Average crop field size**

144 We leveraged the Land Use/Cover Area frame Survey (LUCAS) 2018 Copernicus land cover dataset (d'Andrimont et al., 2021)
145 to estimate the averaged field size in European croplands to decide on the spatial resolution. The LUCAS dataset encompasses



146 63,287 polygons distributed across various land cover types with 120 attributes in Europe, including artificial lands (0.6%),
 147 croplands (34.1%), woodlands (30.0%), shrublands (4.5%), grasslands (28.0%), bare lands (2.5%), wetlands (0.3%) and water
 148 (0.0%). The field sizes of cropland in the LUCAS dataset were labelled as categorical attributes in four levels, including ‘>10
 149 ha’, ‘1-10 ha’, ‘0.5-1 ha’ and ‘<0.5 ha’. We assigned representative values of 15 ha, 5 ha, 0.75 ha and 0.25 ha for each category
 150 (Fig. S9) to approximate the averaged radius of external circles of cropland regions at 0.16 km, varying from 0.03 to 0.22 km
 151 (n=36,199). For simplification, 0.15 km radius (pixel size of 0.3 km) was finally defined as the spatial scale of the Sentinel-2
 152 α_{bs} dataset in this study. Aggregation of 0.01 km observations to 0.3 km is also a strategy to increase temporal Sentinel-2
 153 coverage. While it loses fine-scale details (like hedges, within field heterogeneity), it not only increases the likelihood for
 154 suited conditions for bare soil observations at a given location but also gains robustness, reduces noise, and facilitates
 155 processing.

156 2.1.4 Periods of bare soil exposure

157 To extract periods with bare soil in European cropland regions, we used four spectral indices and their thresholds from previous
 158 analysis (Rizzo et al., 2023), including greenness index (GI) ($GI < 0.65$), normalized difference vegetation index (NDVI) ($-$
 159 $0.05 < NDVI < 0.25$), normalized burn ratio index (NBR) ($NBR > -0.23$) and normalized burn ratio 2 index (NBR2) ($-$
 160 $0.05 < NBR2 < 0.15$). The thresholds of these four indices were determined based on the spectra of 8,005 soil samples collected
 161 globally (Rizzo et al., 2023). In this analysis, these indices were computed from the Sentinel-2 reflectance product on GEE
 162 (Table 1). We further utilized the NDVI and normalized difference snow index (NDSI) to eliminate the periods influenced by
 163 water or snow cover on soils. Dates with NDVI lower than 0 were excluded to avoid water bodies, rocks or other non-vegetated
 164 land surfaces (Korchagina et al., 2020). An NDSI threshold of 0.1 was utilized to obtain snow-free bare soil periods, which is
 165 stricter than the commonly used threshold of 0.4 (Riggs et al., 2016; Härer et al., 2018). Bare soil period is identified if the
 166 conditions of all indices are satisfied. Finally, data points outside mean \pm two standard deviations were considered outliers and
 167 removed.

168 **Table 1** The vegetation index for extracting the bare soil periods in European cropland regions from 2018 to 2020.

Abbreviation	Full name	Formula
GI	Greenness index	$\frac{(2 \times Green) - (Red + Blue)}{(2 \times Green) + (Red + Blue)}$
NDVI	Normalized difference vegetation index	$\frac{NIR - Red}{NIR + Red}$
NBR	Normalized burn ratio index	$\frac{NIR - SWIR2}{NIR + SWIR2}$
NBR2	Normalized burn ratio 2 index	$\frac{SWIR1 - SWIR2}{SWIR1 + SWIR2}$



NDSI	Normalized difference snowing index	$\frac{VIR - SWIR1}{VIR + SWIR1}$
BSI	Bare soil index	$\frac{(SWIR2 + Red) - (NIR + Blue)}{(SWIR2 + Red) + (NIR + Blue)}$

169 The Blue, Green (VIR), Red, NIR, SWIR1 and SWIR2 are represented by bands 2, 3, 4, 8, 11 and 12 of Sentinel-2 products,
 170 respectively.

171 **2.2 Random Forest models for mapping bare soil albedo**

172 **2.2.1 Rationale and design choices**

173 The Sentinel-2 time series over Europe contains frequent gaps due to cloud and snow cover, which hinder regular sampling of
 174 bare soil conditions. To obtain spatiotemporally continuous fields, we used a RF model to learn the relationship between
 175 observed α_{bs} dynamics and potential drivers, thereby extending Sentinel-2 observations in time and space. RF is well-suited to
 176 nonlinear responses, mixed predictors, and heterogeneous sampling, and is widely applied in remote sensing regression and
 177 gap filling (Breiman 2001).

178 **2.2.2 Model inputs and outputs**

179 Two RF models were developed. The first model aimed at predicting the spatial distribution of the temporal average of α_{bs} (α_{bs} ,
 180 *spatial*). Predictions were performed from the following input features: temporal-averaged local solar zenith angle (LSZA), soil
 181 organic carbon (SOC), sand and clay contents, bulk density, pH, temporally averaged soil moisture (SM) and elevation (Table
 182 2).

183 **Table 2.** Features used in the analysis, including satellite properties, atmosphere, soil and surface conditions, as well as country
 184 identity.

Features	Labels	Unit	Spatial resolution	Data source	Classification	Spatial model	Temporal model
local solar zenith angle	LSZA	°	0.3 km	Sentinel-2	Satellite properties	√ (temporal-averaged LSZA at a specific location)	√
time of day	time of day	-	-	Sentinel-2			√



days of year	days of year		-	Sentinel-2		√
soil organic carbon	SOC	g kg ⁻¹	0.25 km	OpenLandMap USDA soil datasets	Soil conditions	√
soil sand content	sand content	%	0.25 km	OpenLandMap USDA soil datasets		√
soil clay content	clay content	%	0.25 km	OpenLandMap USDA soil datasets		√
soil bulk density	bulk density	kg m ⁻³	0.25 km	OpenLandMap USDA soil datasets		√
soil pH	pH	-	0.25 km	OpenLandMap USDA soil datasets		√
soil moisture	SM	cm ³ cm ⁻³	1 km	Global Surface Soil Moisture (GSSM1 km)		√ (temporal-averaged SM at a specific location)
relative soil moisture anomaly	SM_RC	-	1 km	Global Surface Soil Moisture (GSSM1 km)		√
surface elevation	elevation	km	0.03 km	Shuttle Radar Topography Mission (SRTM)	Topography	√
Spatial distribution of α_{bs}	$\alpha_{bs, spatial}$		0.3 km	RF-modeled α_{bs} dataset	Reference	√



186 The second model aimed at predicting the temporal variation of α_{bs} , defined as $\alpha_{bs, temporal} = \alpha_{bs} - \alpha_{bs, spatial}$. The input features of
187 this second model were LSZA, time of day, days of year, relative SM anomaly (SM_RC) and the predicted values of $\alpha_{bs, spatial}$
188 provided by the first RF model (Table 2). All the input features were linearly resampled from the original resolution to 0.3 km
189 pixel size and 5-day temporal resolution to match the pixel size of α_{bs} .

190 The selection of features was based on theoretical and empirical evidence for their potential control on α_{bs} . SOC, sand and clay
191 contents, bulk density and pH affect α_{bs} by modulating soil color, microtopography, surface roughness and water-holding
192 capacity (Cierniewski et al., 2014; Sadeghi et al., 2018; Elfarisna et al., 2024). For example, light-colored sand soil generally
193 has a higher α_{bs} due to larger particles with smoother surfaces, as well as weaker water-holding capacity for reflecting solar
194 radiation, compared to clay and silt (Sun et al., 2015). The elevation, extracted from the digital elevation model (DEM), affects
195 the distribution of incoming solar radiation on the soil and, consequently α_{bs} (Wen et al., 2013). The LSZA, days of year and
196 time of day affect α_{bs} by controlling the direction and the path length of solar radiation in the sun-surface-satellite geometry
197 (Yang et al., 2008). SM is negatively correlated with α_{bs} by changing soil colors and influencing the soil roughness for specific
198 soil types (e.g., dry soil tends to form clods or aggregates, increasing surface roughness) (Gascoïn et al., 2009; Sugathan et al.,
199 2014; Rizzo et al., 2023).

200 The five 0.25 km time-invariant top (upper 30 cm) soil properties (SOC, sand and clay contents, bulk density and pH) were
201 extracted from the U.S. Department of Agriculture (USDA) soil datasets of OpenLandMap (Hengl et al., 2018). The 0.03 km
202 static DEM was obtained from the Shuttle Radar Topography Mission (SRTM) (Farr et al., 2007). The satellite properties
203 (LSZA, days of year and time of day) were derived from Sentinel-2 reflectance products with a 5-day interval and 0.3 km
204 spatial resolution. The SM dataset is from the 1 km daily Global Surface Soil Moisture (GSSM) product (Han et al., 2023),
205 which provides the temporal dynamics of the daily surface soil moisture (0-5 cm) in $\text{cm}^3 \text{cm}^{-3}$, at a coarse spatial resolution of
206 1 km in European scale from 2000 to 2020. GSSM was predicted from machine learning using the datasets of the International
207 Soil Moisture Network, satellite and meteorology (Han et al., 2022).

208 The SM_RC is calculated as the relative deviation from the temporal-averaged SM in each pixel:

$$209 \quad \text{SM_RC}_{i,j} = (\text{SM}_{i,j} - \text{SM}_{\text{ave},j}) / \text{SM}_{\text{ave},j} \quad (2)$$

210 Where $\text{SM}_{i,j}$ and $\text{SM_RC}_{i,j}$ are the SM value and relative SM anomaly at time i in pixel j , respectively. $\text{SM}_{\text{ave},j}$ is the temporal-
211 averaged SM in pixel j .

212 2.2.3 Training and testing of the models

213 The procedure involves hyperparameter tuning, model training and testing. This procedure was implemented to build the two
214 RF models predicting $\alpha_{bs, spatial}$ and $\alpha_{bs, temporal}$.

215 We used a dataset including a total of 75,941 values of the temporal average of α_{bs} for training and testing the first model, and
216 a dataset including a total of 56,754 values of the temporal anomaly of α_{bs} for training and testing the second model. Each
217 dataset was randomly split into two samples: one for training and hyperparameter tuning (80%), and one for out-of-box testing



218 (20%). Hyperparameter tuning was conducted for each model separately, using 10-fold cross-validation with grid searching
219 on the training dataset. Hyperparameters include the number of decision trees (ntrees) from 300 to 1000, and the number of
220 variables sampled (mtry) from 2 to 7 at each split. Specifically, for each pair of hyperparameters (e.g. ntrees of 300 and mtry
221 of 2). The procedure of 10-fold cross-validation is described in Supplementary Text (Text S1.1).

222 With the selected optimal hyperparameters, the RF model was trained on the whole training dataset and hyperparameter tuning
223 sample, and assessed on the out-of-box testing sample using R^2 and RMSE as quality indicators. Overfitting was additionally
224 checked by comparing the final R^2 against the R^2 obtained during cross-validation.

225 The SHAP (SHapley Additive exPlanations) values indicate the contribution of each value for each feature to the individual
226 model prediction by considering all possible combinations of feature subsets (Zhang et al., 2022). The SHAP values of the
227 features in spatial and temporal RF models were induced to visualize the dependencies among features in jointly deciding the
228 α_{bs} variation.

229 **2.2.4 Predicting bare soil albedo over European croplands**

230 The trained spatial and temporal RF models were then applied to produce the 5-day 0.3 km European α_{bs} datasets based on the
231 selected features: (1) LSZA, SM, elevation, SOC, pH, clay content, sand content and bulk density for predicting $\alpha_{bs, spatial}$ with
232 the spatial RF model; (2) LSZA, $\alpha_{bs, spatial}$, SM_RC, days of year, and time of day for predicting $\alpha_{bs, temporal}$ with the temporal
233 RF model. The final continuous spatial-temporal predictions ($\alpha_{bs, RF}$) were derived by adding the predictions of $\alpha_{bs, temporal}$ and
234 $\alpha_{bs, spatial}$, as follows

$$235 \quad \alpha_{bs, RF} = \alpha_{bs, spatial} + \alpha_{bs, temporal} \quad (3)$$

236 **2.3 Independent evaluation datasets**

237 Five types of α_{bs} datasets were utilized to evaluate the performance of the final spatiotemporal albedo predictions ($\alpha_{bs, RF}$) at
238 seven ICOS European cropland sites (BE-Lon, FR-Lam, FR-Aur, FR-EM2, DE-RuS, DE-Geb, DE-Kli), one European Fluxes
239 Database Cluster (EFDC) European cropland site (CZ-KrP), and one Swedish cropland site in Uppsala, and the overall
240 European cropland regions during bare soil periods (Table 3). The bare soil periods at ICOS and EFDC sites were manually
241 identified by checking daily or weekly site photos from 2018 to 2020, selecting periods when the soil within the visual range
242 of the camera was visibly exposed without any covers (Fig. S2). The bare soil periods at Swedish cropland sites were obtained
243 from records directly provided in the literature.

244
245 The α_{bs} datasets of all sites, derived either from site eddy covariance measurements or 5-day 0.3 km Sentinel-2 surface albedo
246 observations, are denoted as $\alpha_{bs, site}$ and $\alpha_{bs, S2}$ to represent the α_{bs} we used for evaluation at site scale in the following text. The
247 $\alpha_{bs, site}$ at the Swedish site, composed of six cropland fields, was extracted from literature directly for comparison (Sieber et al.,



248 2022). We aggregated the field data to represent the $\alpha_{bs, site}$ for this site. The comparison at site scale is only implemented if the
 249 sample size at each site is more than three.

250 We additionally examined the relationships between the daily soil sensor SM measurements and different α_{bs} datasets to
 251 evaluate their consistency in expressing the dependence of α_{bs} on SM, including $\alpha_{bs, RF}$, $\alpha_{bs, MODIS}$, $\alpha_{bs, Gascoin}$, $\alpha_{bs, S2}$ and $\alpha_{bs, site}$
 252 (Table 3).

253 **Table 3.** Evaluation datasets of bare soil albedo (α_{bs}) at sites or European cropland regions from the literature.

α_{bs} evaluation datasets	Formula	Data use	Locations	α_{bs} mean during bare soil periods (mean±standard deviation)	Periods	Data resource	Reference
$\alpha_{bs, site}$	$\alpha_{bs} = \frac{SW_I}{N/SW_O}$ UT	the quality-controlled and gap-filled measurements of the mid-day (11h00-13h00 Central European Summer Time) half-hourly incoming and outgoing shortwave radiation (SW_IN, SW_OUT)	BE-Lon, FR-Lam, FR-Aur, FR-EM2, DE-RuS, DE-Geb, DE-Kli, CZ-KrP	0.13±0.05	2018-2020	ICOS, EFDC	Beeck et al., 2018
-	-	α_{bs} (daily albedo approximated by the ratio of incoming and outgoing shortwave radiation measured at 2-4 minute frequency within three hours of local solar noon)	Ultuna S, Sweden	0.05-0.11 (moist soil) 0.13-0.16 (harrowed and dry soil)	October 2019 - September 2020 (33 individual measurement days)	literature	Sieber et al., 2022
$\alpha_{bs, S2}$	0.3 km 5-day	Sentinel-2 surface albedo	BE-Lon, FR-Lam, FR-Aur, FR-EM2, DE-RuS, DE-Geb, DE-Kli, CZ-KrP,	0.14±0.02	2018-2020	Sentinel-2 surface albedo	Lin et al., 2022



			The southern field of Ultuna in Uppsala in Sweden			product s	
$\alpha_{bs, \text{Gascoin}}$	$\alpha_{bs, \text{Gascoin}} = 0.31e^{-12.7SM} + 0.15$	1 km daily SM dataset	BE-Lon, FR-Lam, FR-Aur, FR-EM2, DE-RuS, DE-Geb, DE-Kli, CZ-KrP, the southern field of Ultuna in Uppsala in Sweden	0.166 ± 0.006	2018-2020	GSSM SM product	Szabó 2024; Han et al., 2022
$\alpha_{bs, \text{MODIS}}$	-	0.5 km daily MODIS surface albedo	BE-Lon, FR-Lam, FR-Aur, FR-EM2, DE-RuS, DE-Geb, DE-Kli, CZ-KrP, the southern field of Ultuna in Uppsala in Sweden	0.160 ± 0.013	2018-2020	MCD43 A3 product	LP DAAC Archive (https://lpdaac.usgs.gov/products/mcd43a3v006/)
$\alpha_{orc, \text{bgd}}$	-	~50 km monthly α_{bs}	cropland regions in Europe	0.133 ± 0.028	2000-2009	product α_{bs} dataset	Pinty et al., 2011
$\alpha_{bs, \text{Carrer}}$	-	~1 km 8-day α_{bs}	cropland regions in Europe	0.121 ± 0.031	2000-2010	product α_{bs} dataset	Carrer et al., 2014

254

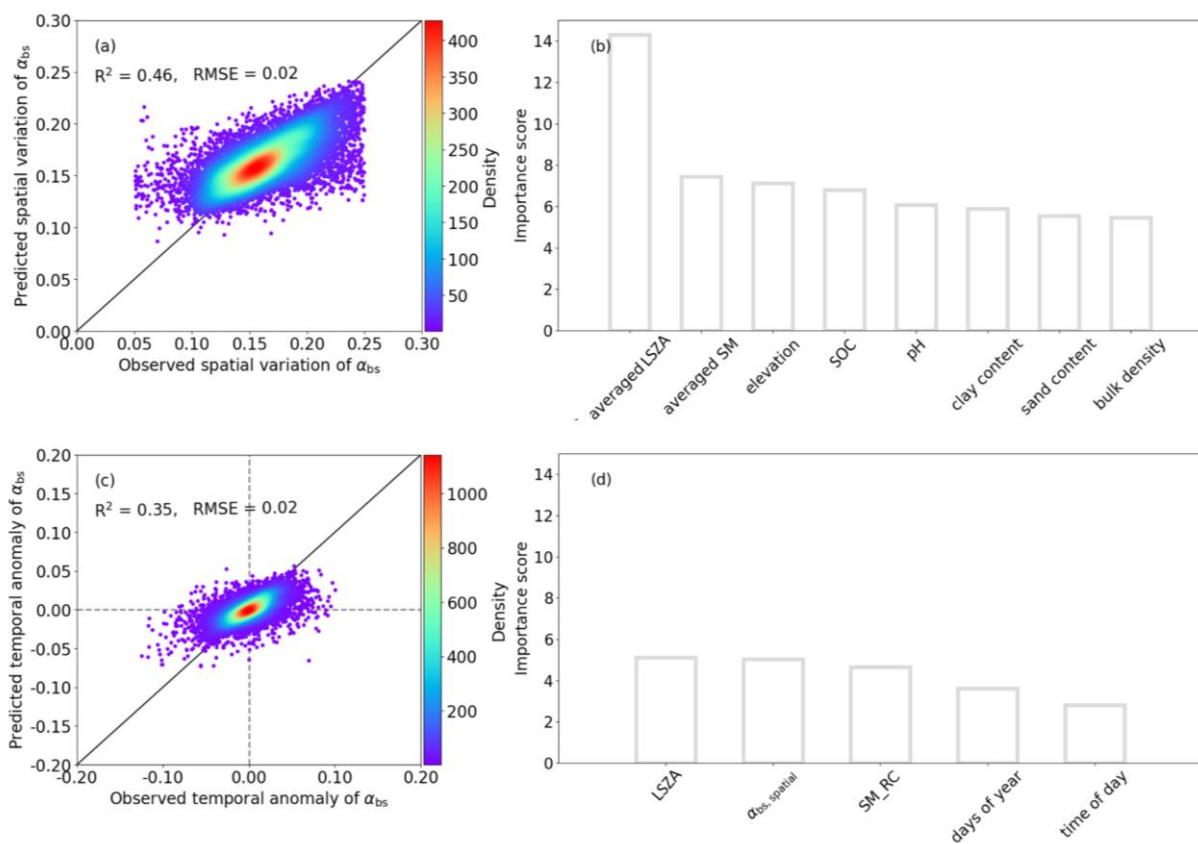
255 3 Results

256 3.1 Controls on spatial and temporal variability of bare soil albedo

257 The random forest models successfully reproduced both the spatial patterns and temporal variability of α_{bs} across European
 258 croplands (Figs. 2a and c), providing a basis for diagnosing the dominant controls on α_{bs} at different scales. The spatial model



259 achieved an R^2 of 0.46, while the temporal anomaly model explained 35 % of the observed variability, with both models
260 yielding RMSEs of 0.02 based on out-of-bag evaluation datasets.

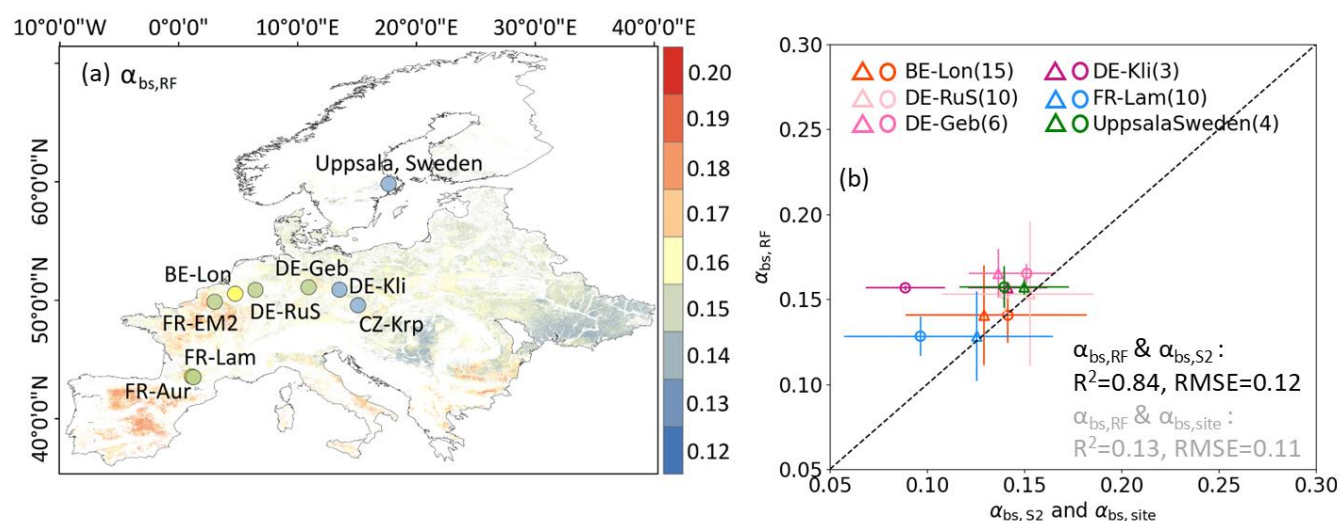


261
262 **Figure 2** The performance of the two random forest models (RF) for predicting European bare soil albedo ($\alpha_{bs, RF}$) in time and
263 space. (a) and (c) are the scatter plots between the predicted and observed spatial bare soil albedo, and between predicted and
264 observed temporal albedo variations from the test dataset, respectively. (b) and (d) are the importance rankings of selected
265 features for spatial and temporal RF modelling. $\alpha_{bs, spatial}$ is the predicted spatial distribution of bare soil albedo. “LSZA, SM,
266 SM_RC, SOC” represent local solar zenith angle (LSZA), soil moisture (SM), relative SM anomaly (SM_RC) and soil organic
267 carbon (SOC), respectively.

268
269 The long-term spatial distribution of α_{bs} ($\alpha_{bs, spatial}$) is primarily controlled by temporally averaged solar zenith angle (LSZA),
270 mean soil moisture conditions and elevation (Fig. 2b). In contrast, temporal variability during bare soil periods is most strongly
271 influenced by instantaneous solar zenith angle, the underlying spatial albedo pattern, and soil moisture anomalies (Fig. 2d).
272 The importance of these variables on α_{bs} has been widely explored in previous studies (Idso et al., 1975; Post et al., 2000; Yang
273 et al., 2008; Gascoïn et al., 2009; Roosjen et al., 2015; Cierniewski et al., 2023). The remaining predictors contribute to weaker



274 but non-negligible impacts. It is reasonable that soil properties (e.g., soil organic carbon, pH) control the spatial distribution
 275 of α_{bs} by adjusting soil colors via the contents of organic matter and nutrients (Sirisathitkul et al., 2025) while time records
 276 adjust its temporal variation (Yu et al., 2024).
 277 Partial dependence analysis further illustrates the physical consistency of these controls. Both LSZA and SM have negative
 278 effects on $\alpha_{bs, spatial}$ and $\alpha_{bs, temporal}$ predictions (Figs. S3a, b, d and f). The elevation increases $\alpha_{bs, spatial}$ by representing specific
 279 soil types with elevation (Fig. S3c) (Badía et al., 2016; Praeg et al., 2020). An impact of $\alpha_{bs, spatial}$ on $\alpha_{bs, temporal}$ is expected as it
 280 represents the location-specific climatic and environmental conditions which are otherwise not represented by the selected
 281 predictors (Fig. S3e).



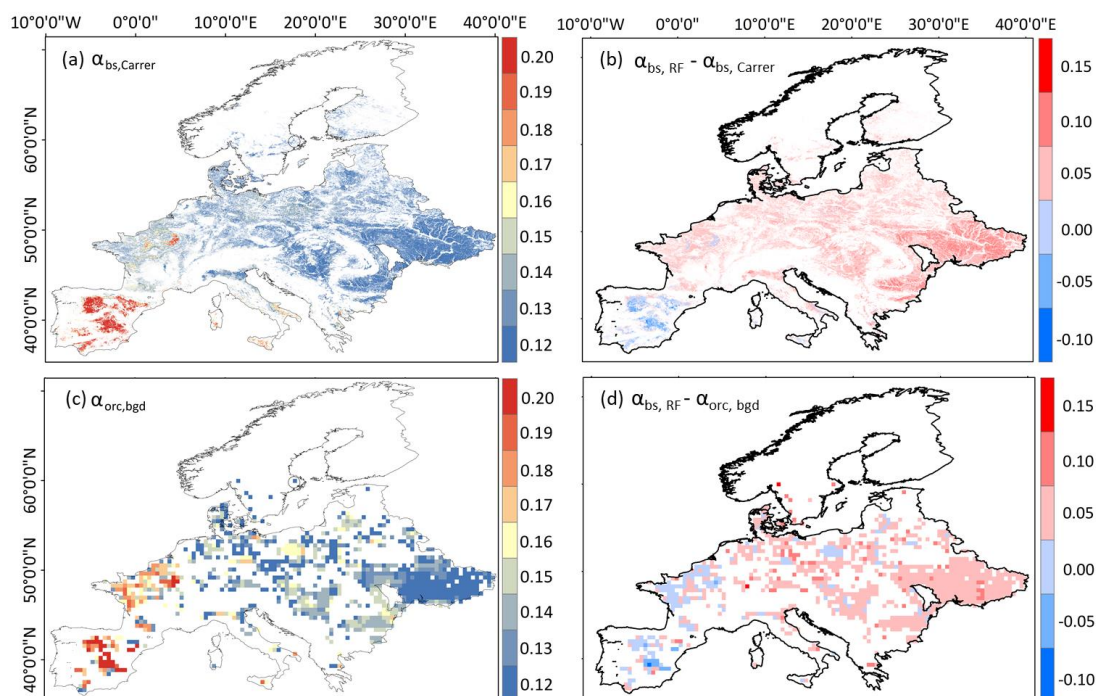
282
 283 **Figure 3** (a) The averaged bare soil albedo (α_{bs}) at 300 m resolution derived from the random forest models over the period
 284 from 2018 to 2020 in the European cropland regions ($\alpha_{bs, RF}$). Dots with colors represent the temporal average of $\alpha_{bs, RF}$ at site
 285 scale; (b) The comparison between $\alpha_{bs, RF}$ and $\alpha_{bs, S2}$ (triangles, with $\alpha_{bs, S2}$ extracted from the Sentinel-2 surface albedo products),
 286 and between $\alpha_{bs, RF}$ and $\alpha_{bs, site}$ (circles, with $\alpha_{bs, site}$ computed from site radiation measurements) at six site fields during the
 287 same bare soil periods. The triangles and circles in different colors correspond to the averages of $\alpha_{bs, RF}$, $\alpha_{bs, S2}$ and $\alpha_{bs, site}$ at
 288 different sites, and the bars represent two standard deviations. The numbers in legend brackets represent the sample size (Table
 289 3 for details). Statistics shown in black indicate the correlation passes the significance level of 0.05 ($p < 0.05$), while the one in
 290 gray indicates non-significance ($p > 0.05$).

291 3.2 European-scale spatial pattern of bare soil albedo

292 The spatiotemporal average of $\alpha_{bs, RF}$ is 0.15 ± 0.01 over European cropland from 2018 to 2020 which is within the range of α_{bs}
 293 found in the literature, which spans from 0.15 to 0.22 derived from 7,537 European topsoil samples in 2022 (Szabó et al.,
 294 2024). Our α_{bs} dataset has a higher spatiotemporal average than earlier products including $\alpha_{bs, Carrer}$ of 0.12 ± 0.03 (2001-2010)
 295 and $\alpha_{orc, bgd}$ of 0.13 ± 0.03 (2000-2009), respectively, which have coarser spatial resolutions of 1 km and ~ 55.5 km (Figs. 4 and



296 S4) (Carrer et al., 2014; He et al., 2019). The distribution of the final predictions $\alpha_{bs, RF}$ was similar to the distribution of the
297 α_{bs} data extracted from Sentinel-2 observations by vegetation indices within European cropland regions from 2018 to 2020
298 (Fig. S4). This indicates that our predictions cover the spatio-temporal variations in European croplands.
299 The multi-year spatial pattern exhibits broad west-east and north-south gradients (Fig. 3a) that align with major soil zones,
300 with darker surfaces where organic matter is higher and brighter surfaces where carbonates are more prevalent, a contrast
301 repeatedly reported for European croplands (Carrer et al., 2018; Rizzo et al., 2023). The Iberian Peninsula, southwestern and
302 southern France, and the Mediterranean coastal regions have bright soils with α_{bs} of 0.18-0.20. While the soil in north-central
303 and eastern Europe (e.g., Germany and Poland) is dark with α_{bs} of 0.12-0.15.
304 Despite general agreement in continental-scale gradients, spatial correlations between our field-scale $\alpha_{bs, RF}$ estimates and
305 existing coarse-resolution products remain low (Pearson $r = 0.07$ -0.15; Fig. 4).



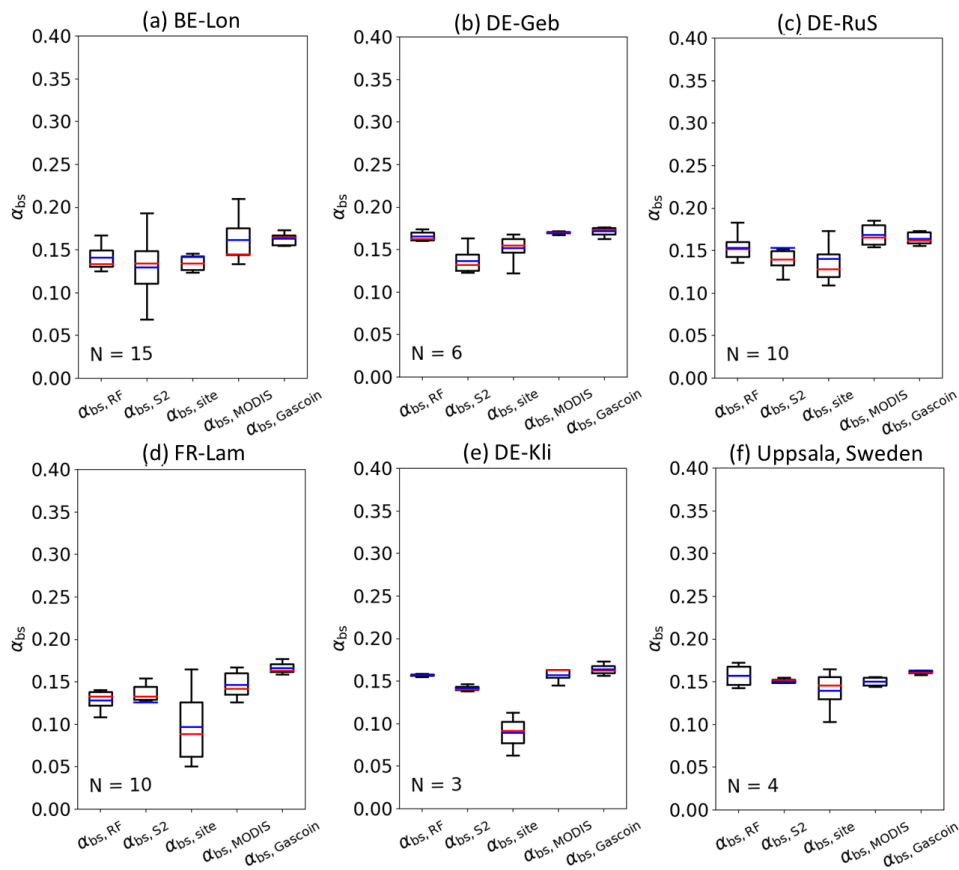
306
307 **Figure 4** The spatial comparison between the new albedo product $\alpha_{bs, RF}$ and two existing bare soil albedo products in European
308 cropland scale. (a) the averaged ~1 km 8-day European bare soil albedo dataset from 2000 to 2010 ($\alpha_{bs, Carrer}$); (b) the difference
309 between the averaged 2018-2020 $\alpha_{bs, RF}$ and the averaged 2001-2010 $\alpha_{bs, Carrer}$; (c) the averaged ~50 km monthly bare soil albedo
310 dataset from 2001 to 2009 ($\alpha_{orc, bgd}$); (d) the difference between the averaged 2018-2020 $\alpha_{bs, RF}$ and the averaged 2001-2009 $\alpha_{orc,}$
311 bgd .

312 3.3 Site-scale characteristics of bare soil albedo



313 During bare soil windows, $\alpha_{bs, RF}$ has an average of 0.15 ± 0.01 across six eddy-covariance cropland sites, with time series
314 showing coherent field-scale dynamics (Figs. 3b and 6). Time series of $\alpha_{bs, RF}$ exhibit site-specific background levels with
315 short-term fluctuations.

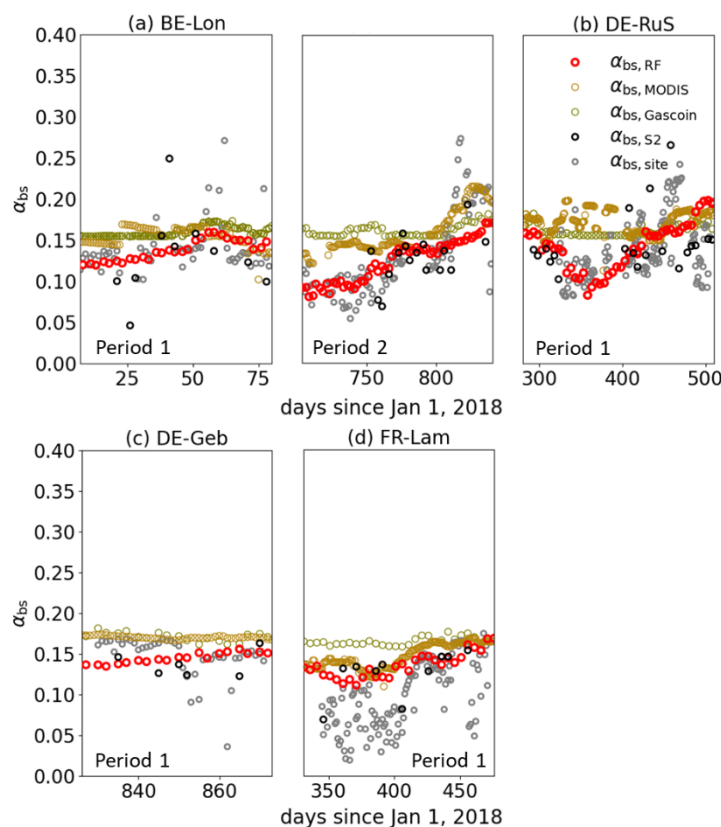
316 The daily $\alpha_{bs, site}$ and $\alpha_{bs, S2}$ at the sites, for which bare soil albedo estimates were available, were utilized to compare with daily
317 variations in $\alpha_{bs, RF}$ (Figs. 5 and 6). Results show that the time-averaged predicted albedo was close to observation ($R^2=0.84$,
318 $RMSE=0.12$ for comparison with $\alpha_{bs, S2}$), while the agreement with in site observations is weaker ($R^2=0.12$, $RMSE=0.11$ for
319 comparison with $\alpha_{bs, site}$) (Fig. 3b). $\alpha_{bs, RF}$ is $+21.87 \pm 27.71\%$ (mean \pm standard deviation) higher than $\alpha_{bs, site}$ (0.14 ± 0.02) for the
320 same periods (Figs. 5 and 6). While the difference between $\alpha_{bs, RF}$ and underlying training data ($\alpha_{bs, S2}$, 0.12 ± 0.02) across sites
321 is smaller ($+7.11 \pm 3.55\%$). It implies that the difference between $\alpha_{bs, RF}$ and $\alpha_{bs, site}$ is a mix of biases in the RF to capture
322 Sentinel-2 observations and differences between $\alpha_{bs, S2}$ from $\alpha_{bs, site}$. We also found that the difference of the model predictions
323 between $\alpha_{bs, RF}$ and $\alpha_{bs, site}$ varies across different soil types. BE-Lon, FR-EM2 and FR-Lam sites, belonging to alfisols (light
324 brown to reddish-brown), have lower bias compared with site measurements (Fig. 3). While DE-Geb and DE-Kli (dark brown
325 to black molisols) and CZ-KrP (brown to yellowish-brown inceptisols) induce higher differences from measurements.



326



327 **Figure 5** The boxplots of $\alpha_{bs, RF}$, $\alpha_{bs, MODIS}$, $\alpha_{bs, Gascoin}$, $\alpha_{bs, S2}$ and $\alpha_{bs, site}$ at six cropland sites during the same bare soil periods
328 from 2018 to 2020. The values of $\alpha_{bs, RF}$ are the bare soil albedo derived from the spatiotemporal random forest models. The
329 values of $\alpha_{bs, S2}$ are extracted from the Sentinel-2 surface albedo products, while the values $\alpha_{bs, site}$ are computed by site eddy
330 covariance measurements (see Table 3). The values of $\alpha_{bs, MODIS}$ are extracted from 500m daily MODIS surface albedo product
331 (MCD43A3). $\alpha_{bs, Gascoin}$ are computed by the exponential function of SM using the 1 km GSSM SM product (see Table 3). The
332 red and blue lines in each figure represent the median and mean values, respectively.
333



334
335 **Figure 6** Values of $\alpha_{bs, RF}$, $\alpha_{bs, MODIS}$, $\alpha_{bs, Gascoin}$ at four sites during the same bare soil periods from 2018 to 2020, compared with
336 $\alpha_{bs, S2}$ and $\alpha_{bs, site}$ (see Table 3). Values of $\alpha_{bs, RF}$ are the bare soil albedo derived from the spatiotemporal random forest models
337 (red hollow dots). Values of $\alpha_{bs, S2}$ are extracted from the Sentinel-2 surface albedo products (black hollow dots), while $\alpha_{bs, site}$
338 values are computed by site radiation measurements (gray hollow dots). The values of $\alpha_{bs, MODIS}$ are extracted from 500 m daily
339 MODIS surface albedo product (MCD43A3) (yellow hollow dots). The values of $\alpha_{bs, Gascoin}$ are computed by the function of
340 soil moisture (SM) using the 1 km GSSM SM product (brown hollow dots). 'Period X' in each plot indicates the bare soil
341 period identified by daily or weekly site photos. Plot in-between (a) and (b) belongs to BE-Lon site but in Period 2.
342



343 For reference, $\alpha_{bs, \text{Gascoin}}$ (0.17 ± 0.01) and $\alpha_{bs, \text{MODIS}}$ (0.16 ± 0.02) are higher than $\alpha_{bs, \text{RF}}$ and $\alpha_{bs, \text{site}}$ at the same sites and times (Fig.
344 5). Correlation analyses showed that temporal variations in $\alpha_{bs, \text{RF}}$, as prescribed by Eq. (3), tracked soil moisture dynamics
345 ($R^2=0.51$, $\text{RMSE}=0.006$), which is darkening after wetting and progressive brightening during dry-downs (Fig. S7). This
346 correspondence is stronger than $\alpha_{bs, \text{site}}$ ($R^2=0.30$, $\text{RMSE}=0.02$) and $\alpha_{bs, \text{S2}}$ ($R^2=0.06$, $\text{RMSE}=0.01$), comparable to $\alpha_{bs, \text{MODIS}}$
347 ($R^2=0.46$, $\text{RMSE}=0.007$), and weaker than $\alpha_{bs, \text{Gascoin}}$ ($R^2=0.94$, $\text{RMSE}=0.001$). The particularly high correlation for $\alpha_{bs, \text{Gascoin}}$
348 is expected because $\alpha_{bs, \text{Gascoin}}$ is directly derived from soil moisture. Compared with $\alpha_{bs, \text{site}}$, $\alpha_{bs, \text{RF}}$ is consistently brighter across
349 the soil moisture range (~ 0.01 - 0.02 higher in α_{bs}), with the positive bias most pronounced for soil moisture $> 50\%$. $\alpha_{bs, \text{RF}}$ also
350 exhibits a smaller amplitude and variance than $\alpha_{bs, \text{site}}$, smoothing the peak darkening seen in the site observations.

351 4 Discussion

352 4.1 Characteristics of the reconstructed bare soil albedo

353 The reconstructed α_{bs} is designed to capture the dominant physical controls on bare soil albedo while balancing the trade-offs
354 behind continuity and representativeness based on Sentinel-2 reflectance. It enables the characterization of bare soil albedo
355 variability at spatial and temporal scales relevant for agricultural surface energy exchange across Europe. Compared with
356 earlier continental-scale estimates ($\alpha_{orc, \text{bgd}}$ and $\alpha_{bs, \text{Carrer}}$), the reconstructed α_{bs} resolves sub-kilometer heterogeneity that is
357 critical for diagnosing field-scale radiative contrasts in fragmented cropland landscapes (Pinty et al., 2011; Carrer et al., 2014;
358 He et al., 2019).

359 The differences among estimates could be attributed to differences in the periods covered: 2001-2009 for $\alpha_{orc, \text{bgd}}$, 2001-2010
360 for $\alpha_{bs, \text{Carrer}}$, and 2018-2020 for $\alpha_{bs, \text{RF}}$. Changes in climate and environmental conditions during these periods, such as the
361 observed decreasing trend of soil moisture on a European scale from 1991 to 2020 compared to 1991, especially in central and
362 eastern Europe (Almendra-Martín et al., 2022), can theoretically result in average higher 2018-2020 α_{bs} compared to the period
363 before 2010.

364 The estimation of α_{bs} largely reflects the seasonal variability of α_{bs} in European cropland fields (Fig. 6), providing a basis to
365 quantify measures for radiation management in agriculture (Yu et al., 2024). This dataset reduces sampling discontinuities
366 associated with cloud cover, snow, and vegetation masking (Figs. 6, S1 and S2), allowing seasonal envelopes and inter-site
367 contrasts in α_{bs} to be examined more consistently (Wang et al., 2025). The selected features for RF models enable α_{bs} prediction
368 in regions with limited satellite observations due to cloud cover or aerosols, because the necessary predictors of the RF model,
369 including soil properties and solar-surface-satellite geometry, are not affected by atmospheric conditions (Figs. 2b and d).

370 4.2 Physical controls of the reconstructed bare soil albedo

371 Overall, the results indicate that variability in bare soil albedo are mainly related to soil properties and radiative geometry,
372 while short-term variability is driven by soil moisture dynamics.



373 We isolated and quantified the contributions of soils, weather and management on spatio-temporal variations in bare soil
374 albedo. It reveals that the α_{bs} dynamics arise from the interplay of multiple controls rather than any single dominant driver
375 (Yang et al., 2008). Temporal changes ($\alpha_{bs, temporal}$) are primarily associated with variations in soil moisture and local solar
376 zenith angle, with additional seasonality represented by time-of-day and day-of-year terms (Fig. 3b). This underscores the role
377 of short-term variations in illumination geometry and surface wetness in shaping bare soil albedo dynamics (Yu et al., 2024).
378 Whereas spatial contrasts ($\alpha_{bs, spatial}$) reflect long-term patterns associated with soil moisture and solar geometry, further
379 modulated by invariant factors such as elevation and soil type (Fig. 3d). This suggests that stable radiative conditions and soil-
380 related properties (e.g., soil organic carbon and pH) exert dominant controls on large-scale albedo variability (Sirisathitkul et
381 al., 2025). Approaches that rely solely on soil moisture as drivers of α_{bs} (Gascoïn et al., 2009) are thus likely to misestimate
382 α_{bs} such as overestimating α_{bs} during dry-down over dark, carbon-rich Mollisols, and underestimating α_{bs} during wet periods
383 under low solar zenith angles, when viewing geometry elevates apparent reflectance.

384 Soil moisture acts as a short-term control on α_{bs} by changes in soil color and soil roughness through wetting, darkening and
385 dry-down brightening (Rizzo et al., 2023). The impact of local solar zenith angle is expected due to its impact on the relative
386 position between the spaceborne sensor and the observed areas, affecting the amount of reflected solar radiation (Yang et al.,
387 2008): a small zenith angle (e.g., 25°) results in nearly vertical solar radiation reflectance and a high α_{bs} (Fig. S3a). It is treated
388 as a physical control on the measured radiative signal (Liu et al., 2009). Its contribution is separate from soil moisture and soil
389 properties and reflects the presence of sun-surface-satellite geometry rather than a proxy of unavailable factors, meaning that
390 α_{bs} can be understood in light of seasonal changes in observation geometry as well as surface state.

391 Soil properties explain much of the stable spatial structure onto which moisture and geometry act (Rizzo et al., 2023). Variables
392 such as elevation or bulk density do not change α_{bs} directly but act as proxies for topographic setting or soil structure where
393 more specific drivers (e.g., aspect or slope at the same scale) are not available in the RF model (Figs. 2b and d). For instance,
394 higher elevations generally have lighter soil colors, which might increase $\alpha_{bs, spatial}$ (Fig. S3c) (Badía et al., 2016; Praeg et al.,
395 2020). Because of the collinearity of bulk density and clay content (Heuscher et al., 2005), their importance reflects predictive
396 utility rather than causal influence on α_{bs} . They stabilize spatial patterns and improve field coherence, not to assign mechanistic
397 primacy. A day-of-year term is included to capture recurring within-year patterns that arise from sunlight, crop calendars, and
398 hydro-meteorology (Reichstein et al., 2019). Since the same day-of-year repeats across years, this term is not intended to
399 encode year-specific events. It provides a seasonal envelope that supports interpolation and extension. A consequence is that
400 unusual events that deviate strongly from the typical seasonal trajectory can be damped in the reconstructed series, even if they
401 appear clearly in individual clear-sky observations.

402 Although soil type is related to soil albedo (Post et al., 2000; Rizzo et al., 2023), we excluded it from the RF because of the
403 coarse soil type map (~ 55.5 km, USDA 2023) and due to significant within soil type variation of surface soil color (not shown).
404 Site comparison reveals that the model performs well for soils of intermediate brightness, but its errors increase for very dark
405 or very bright soils (Fig. 3b). This result indicates that the soil type carries information not captured by bulk density, clay, sand,



406 or SOC (e.g., mineral composition and the type of organic matter). It also implies that the importance rankings of predictors
407 influencing α_{bs} may exhibit spatiotemporal heterogeneity.

408 **4.3 Limitations**

409 Despite the process-oriented reconstruction of bare soil albedo across European croplands, several limitations remain,
410 primarily associated with situations in which surface heterogeneity or dynamics operate at spatial or temporal scales finer than
411 those resolved by the available predictors.

412 First, the mismatched scales between field and satellite observations introduce representativeness errors. $\alpha_{bs, site}$ is representative
413 for 8-1000 m² (Eichler 2022) and satellite-based $\alpha_{bs, RF}$ is for 90000 m². Soils might show substantial variation in soil properties
414 such as texture, color, crusting, residue, and moisture at the scales of meters (Charles et al., 2007), and the bare soil fraction
415 within a 0.3 km footprint can shift rapidly during sowing and post-harvest. Thus, the resulting $\alpha_{bs, RF}$, possibly represents an
416 area-weighted mixture of exposed soil, crop residues, and smooth signals of α_{bs} dynamics (Yue et al., 2020; Dai et al., 2022;
417 Yu et al., 2024).

418 Second, a sampling bias exists in the training data as periods with crop, clouds or snow covers with extreme soil moisture
419 conditions were excluded. Bare soil is often exposed in autumn or winter periods, only about 35 days in each year from
420 Sentinel-2 data averaged at the 8 ICOS sites satisfied our criteria (Figs. S1 and S2). Fixed local overpass time of Sentinel-2
421 (~10:30) provides sparse directional sampling of α_{bs} at the pixel level. Thus, anisotropy is averaged and variance related to
422 extreme cases in the subfield is reduced, with a tendency to underestimate high-magnitude fluctuations (Figs. 2, 5 and 6), such
423 as few observed $\alpha_{bs, S2}$ during the periods of 2019 winter at BE-Lon, DE-RuS, and FR-Lam sites (Figs. 6a, b and d) (Sudmanns
424 et al., 2019; Harmel et al., 2018).

425 Third, base soil masking is not perfect. Crop residue visible or occasional sparse regrowth normally have a higher albedo than
426 the soil (Fig. S5) (Yu et al., 2024), while surface shadows created by terrain or clouds exhibit low reflectance similar to dark
427 soil (Qiu et al., 2019). Using multiple indices in this analysis mitigates but does not eliminate these confusions entirely.

428 Fourth, the selection of predictors in the RF model might induce uncertainty. The use of coarse resolution (1 km) soil moisture
429 data together with high resolution data could have led to an underestimation of the effect of spatial variation of soil moisture
430 on α_{bs} . A test of adding soil moisture as a predictor for $\alpha_{bs, spatial}$ led to the elimination of it during the feature elimination
431 procedure, which deviated from the earlier findings of a well-known negative correlation of spatial patterns of soil moisture
432 and α_{bs} (Gascoïn et al., 2009). Compared with the stable seasonal variation of local solar zenith angle, soil moisture has a
433 higher potential to be disturbed by the environment such as cloud or snow covering periods, which adds noise and reduces the
434 explanatory power. It might explain the higher ranking of local solar zenith angle than soil moisture in predicting $\alpha_{bs, RF}$ (Figs.
435 2b and d). In theory, the relative contribution of these two predictors depends on specific scenarios. The comparably higher
436 importance of zenith angle in this study should not be taken to mean that soil moisture is intrinsically less influential in
437 controlling α_{bs} (Yang et al., 2008; Roosjen et al., 2015). In addition, very sharp post-event shifts of α_{bs} , especially caused by



438 frequent agricultural activities in sub-regions such as irrigation or tillage, can be muted if the relevant proxy indicators are
439 missing in RF (Mohr et al., 2023; Yu et al., 2024; Goodwell et al., 2025). In their absence, the model smooths these rapid
440 dynamics and underestimates the abrupt changes in α_{bs} , yielding a weak response (Figs. 2a and c). Uncertainty of predicted α_{bs} ,
441 α_{RF} therefore increases when these rapid physical changes occur on the surface.

442 Collectively, these scale and sampling properties explain why $\alpha_{\text{bs, RF}}$ preserves seasonal envelopes and regional patterns yet
443 under-represents rapid, high-magnitude extremes. These limitations also highlight the need for future integration of higher-
444 resolution meteorological and soil moisture products, improved surface characterization, and more continuous albedo
445 observations to better capture short-term variability in agricultural landscapes.

446 5 Conclusion

447 By integrating explicit bare soil screening of Sentinel-2 surface albedo observation with a random forest reconstruction
448 framework, this study provides a spatially explicit and temporally continuous estimate of bare soil albedo across European
449 croplands at field-relevant scales. The reconstructed dataset captures the pronounced seasonal variability in bare soil albedo
450 and exhibits spatial patterns. Contrary to our initial expectation that soil properties control the spatial distribution, they define
451 relatively stable spatial contrasts in bare soil albedo, without dominating the predictor importance rankings. Additional spatial
452 variability is explained by radiative geometry and temporally averaged soil moisture. The temporal evolution of the estimated
453 soil albedo shows improved coherence with site-scale measurements compared to existing continental satellite products,
454 particularly in resolving seasonal dynamics of soil albedo. This result further indicates that short-term temporal variations are
455 more closely linked to fluctuations in soil moisture than to static soil properties, while variations in solar radiation act as a
456 secondary modulating factor, thereby supporting our second hypothesis regarding the drivers of temporal dynamics.

457 While uncertainties remain under conditions of rapid surface change such as immediately following rainfall or irrigation events,
458 residue redistribution, or tillage, these limitations primarily reflect constraints in observational sampling and predictor
459 resolution rather than inconsistencies in the reconstructed patterns. Such uncertainties are expected to diminish with the
460 integration of higher-resolution hydrometeorological drivers (e.g., soil moisture) and denser temporal sampling of bare soil
461 conditions. Overall, the dataset is well-suited for characterizing seasonal bare soil albedo variability across heterogeneous
462 agricultural landscapes.

463 Quantifying high spatiotemporal bare soil albedo provides a physically grounded basis to diagnose the seasonal water and
464 energy dynamics that couple agriculture to climate, especially in agroecosystem modelling. Bare soil albedo directly modulates
465 surface radiation partitioning, influencing soil temperature, evaporation, near-surface energy exchange, and cropland-climate
466 coupling. Incorporation of daily bare soil albedo information into land surface and agroecosystem models has the potential to
467 improve simulations of short-term thermal and moisture dynamics, which are poorly represented when albedo is prescribed at
468 coarse spatial resolution or monthly time steps. Existing modelling approaches typically rely on static or climatological
469 representations of bare soil albedo, limiting their ability to capture rapid transitions that arise from soil wetting-drying cycles



470 and agricultural management. Comparably, the reconstructed albedo presented has more stable temporal evolutions and
471 smoother trends. Incorporating daily bare soil albedo into surface energy balance frameworks enable these dynamics to be
472 explicitly represented, offering new opportunities to diagnose surface energy feedbacks, thereby improving the simulation of
473 temperature stress on plants and soil organisms. Such diagnostics are not attainable with monthly bare soil albedo products
474 due to its temporal aggregation effect. With planned temporal extension and application beyond Europe, this reconstructed
475 bare soil albedo opens new opportunities for climate assessment, crop system evaluation across large spatial and temporal
476 scales, thereby facilitating climate-smart cropland management.

477 **5 Code/Data availability**

478 The bare soil albedo dataset for European cropland regions from 2018 to 2020, with a spatial resolution of 0.3 km and a time
479 step of 5 days, is freely available at <https://doi.org/10.6084/m9.figshare.30488027.v1> (Yu et al., 2025). The data is stored in a
480 zip archive <albedo_bs_RF.zip> in GeoTiff format, organized into three subfolders by year. An example file name of
481 “bsa_spatiotemporal_2018_01_01” means $\alpha_{bs, RF}$ on January 1, 2018. The coordinate system is WGS84 (“EPSG:4326”).
482 Observation dataset from Sentinel-2 product used for training and testing in the spatial and temporal RF models are provided
483 as <Training_RF_spatial.csv> and <Training_RF_temporal.csv>. We run all models on the R programming Language, which
484 are named as <s2albedo-RF-spatial.R> and <s2albedo-RF-temporal.R>. The observation dataset and codes can be derived
485 from the link above.

486 **Author contributions**

487 K.Y., D.S.G. and Y.S. conceived the idea and designed the study. K.Y. processed all data, produced the dataset and initiated
488 the manuscript. D.S.G., P.C., and R.L. supervised the study. D.M. improved the methodology. S.W. contributed to the data
489 processing. D.S.G., Y.S., P.C., R.L., D.M., T.S., S.W., P.S., and C.Z. contributed to the data processing, result analysis, and
490 the manuscript improvements.

491 **Competing interests**

492 Some authors are members of the editorial board of journal Biogeosciences.

493 **Acknowledgments**

494 We acknowledge support from the ClieNFarms project (Grant Agreement ID: 101036822). We thank Eric Ceschia, Tiphaine
495 Tallec, Aurore Brut, Bernard Heinesch, Christian Brümmer, Frederik Schrader, Marius Schmidt, Manuel Acosta, Pauline
496 Buysse, and Thomas Gruenwald of ICOS and EFDC stations for providing the ecosystem flux datasets used in our validation
497 process. We are grateful to Gaétan Pique and Dominique Carrer for providing the produced European bare soil albedo map for



498 our comparison process. We thank ChatGPT for assistance with English editing, proofreading, and improving the clarity of
499 the manuscript.



500 References

- 501 Amazirh, A., Bouras, E. H., Olivera-Guerra, L. E., Er-Raki, S., and Chehbouni, A.: Retrieving crop albedo based on radar
502 Sentinel-1 and random forest approach, *Remote Sens.*, 13, 3181, doi: 10.3390/rs13163181, 2021.
- 503 Almendra-Martín, L., Martínez-Fernández, J., Piles, M., González-Zamora, A., Benito-Verdugo, P., and Gaona, J.: Analysis
504 of soil moisture trends in Europe using rank-based and empirical decomposition approaches, *Global Planet. Change*, 215,
505 103868, doi: 10.1016/j.gloplacha.2022.103868, 2022.
- 506 Allen, L., de Benoist, B., Dary, O., and Hurrell, R.: Guidelines on food fortification with micronutrients, World Health
507 Organization and Food and Agricultural Organization of the United Nations, Geneva, 2006.
- 508 Bright, R. M., Zhao, K., Jackson, R. B., and Cherubini, F.: Quantifying surface albedo and other direct biogeophysical climate
509 forcings of forestry activities, *Glob. Change Biol.*, 21, 3246-3266, doi: 10.1111/gcb.12951, 2015.
- 510 Bsaibes, A., Courault, D., Baret, F., Marie, W., Oliso, A., Jacob, F., Olivier, H., Marloie O., Bertrand, N., Desfond, V., and
511 Kzemipour, F.: Albedo and LAI estimates from FORMOSAT-2 data for crop monitoring, *Remote Sens. Environ.*, 113, 716-
512 729, doi: 10.1016/j.rse.2008.12.005, 2009.
- 513 Bablet, A., Vu, P.V.H., Jacquemoud, S., Viallefont-Robinet, F., Fabre, S., X. Briottet, X., Sadeghi, M., Whiting, M.L., Baret,
514 F., and Tian, J.: MARMIT: A Multilayer Radiative Transfer Model of Soil Reflectance to Estimate Surface Soil Moisture
515 Content in the Solar Domain (400–2500 nm), *Remote Sens. Environ.* 217, 1-17, doi: 10.1016/j.rse.2018.07.031, 2018.
- 516 Buster, G., Benton, B.N., Glaws, A., and King, R. N.: High-resolution meteorology with climate change impacts from global
517 climate model data using generative machine learning, *Nat. Energy*, 9, 894-906, doi: 10.1038/s41560-024-01508-0, 2024.
- 518 Badía, D., Ruiz, A., Girona, A., Martí, C., Casanova, J., Ibarra, P., and Zufiaurre, R.: The influence of elevation on soil
519 properties and forest litter in the Siliceous Moncayo Massif, SW Europe, *J. Mt. Sci.*, 13, 2155-2169, doi: 10.1007/s11629-016-
520 3955-5, 2016.
- 521 Breiman, L.: Random forests, *Mach. Learn.*, 45, 5-32, doi: 10.1023/A:1010933404324, 2001.
- 522 Beeck, M., Gielen, B., Merbold, L., Ayres, E., Serrano-Ortiz, P., Acosta, M., Pavelka, M., Montagnani, L., Nilsson, M.,
523 Klemedtsson, L., Vincke, C., De Ligne, A., Moureaux, C., Marañón-Jimenez, S., Saunders, M., Mereu, S., and Hörtnagl, L.:
524 Soil-meteorological measurements at ICOS monitoring stations in terrestrial ecosystems, *Int. Agrophys.*, 32, 619-631, doi:
525 10.1515/intag-2017-0049, 2018.
- 526 Copernicus Sentinel-2 (processed by ESA): MSI Level-2A BOA Reflectance Product, Collection 1, European Space Agency,
527 doi: 10.5270/S2_-zkn9xjsj, 2021.
- 528 Cheng, J., and Liang, S.: Estimating the broadband longwave emissivity of global bare soil from the MODIS shortwave albedo
529 product, *J. Geophys. Res. Atmos.*, 119, 614-634, doi: 10.1002/2013JD020505, 2014.
- 530 Cierniewski, J., Karnieli, A., Kaźmierowski, C., and Ceglarek, J.: A tool for predicting diurnal soil albedo variation in Poland
531 and Israel, *EARSel eProceedings*, 13, 36-40, doi: 10.12760/02-2014-1-07, 2014.



- 532 Cierniewski, J., Ceglarek, J., Karnieli, A., and Królewicz, S., Kaźmierowski, C., Zagajewski, B.: Predicting the diurnal blue-
533 sky albedo of soils using their laboratory reflectance spectra and roughness indices, *J. Quant. Spectrosc. Radiat. Transf.*, 200,
534 25-31, doi: 10.1016/j.jqsrt.2017.06.002, 2017.
- 535 Cierniewski, J., Ceglarek, J., and Kazmierowski, C.: Estimating the diurnal blue-sky albedo of soils with given roughness
536 using their laboratory reflectance spectra. *J. Quant. Spectrosc. Radiat. Transfer.* 217, 213-223, doi: 10.1016/j.jqsrt.2018.06.003,
537 2018.
- 538 Cierniewski, J., and Ceglarek, J.: Influence of arable land location incorporating its roughness on blue-sky albedo variation, *J.*
539 *Quant. Spectrosc. Radiat. Transf.*, 296, 108440, doi: 10.1016/j.jqsrt.2022.108440, 2023.
- 540 Carrer, D., Roujean, J. L., and Meurey, C.: Comparing operational MSG/SEVIRI land surface albedo products from Land SAF
541 with ground measurements and MODIS, *IEEE Trans. Geosci. Remote Sens.*, 48, 1714-1728, doi:
542 10.1109/TGRS.2009.2034530, 2010.
- 543 Carrer, D., Meurey, C., Ceamanos, X., Roujean, J. L., Calvet, J. C., and Liu, S. L.: Dynamic mapping of snow-free vegetation
544 and bare soil albedos at global 1 km scale from 10-year analysis of MODIS satellite products, *Remote Sens. Environ.*, 140,
545 420-432, doi: 10.1016/j.rse.2013.09.005, 2014.
- 546 Canisius, F., Wang, S. S., Croft, H., Leblanc, S. G., Russell, H. A. J., Chen, J., and Wang, R.: A UAV-based sensor system for
547 measuring land surface albedo: tested over a boreal peatland ecosystem, *Drones*, 3, 27, doi: 10.3390/drones3020027, 2019.
- 548 Dai, Z. W., Ding, Y. L., Xu, C., Chen, Y. H., and Liu, L.: Evaluation of the impact of crop residue on fractional vegetation
549 cover estimation by vegetation indices over conservation tillage cropland, *Int. J. Remote Sens.*, 43, 9454-9479, doi:
550 10.1080/01431161.2022.2151432, 2022.
- 551 d'Andrimont, R., Verhegghen, A., Meroni, M., Lemoine, G., Strobl, P., Eiselt, B., Yordanov, M., Martinez-Sanchez, L., and
552 van der Velde, M.: LUCAS Copernicus 2018: Earth-observation-relevant in situ data on land cover and use throughout the
553 European Union, *Earth Syst. Sci. Data*, 13, 1119-1133, doi: 10.5194/essd-13-1119-2021, 2021.
- 554 Davin, E. L., Seneviratne, S. I., Ciais, P., Olioso, A., and Wang, T.: Preferential cooling of hot extremes from cropland albedo
555 management, *Proc. Natl. Acad. Sci. USA*, 111, 9757-9761, doi: 10.1073/pnas.1317323111, 2014.
- 556 Eichler, S. E.: Portable apparatus for high spatial and temporal resolution of in situ real-time surface albedo measurement in
557 agricultural fields, *Environ. Sci. Adv.*, 1, 297-304, doi: 10.1039/D2VA00003A, 2022.
- 558 Elfarisna, E., Rahmayuni, E., Herman, W., Putri, E. L., and Kurniati, K.: Soil organic matter and its correlation with several
559 chemical properties of Inceptisols in rice fields in Java, *Univ. J. Agric. Res.*, 12, 242-248, doi: 10.13189/ujar.2024.120603,
560 2024.
- 561 Farr, T. G., Rosen, P. A., Caro, E., Crippen, R., Duren, R., Hensley, S., Kobrick, M., Paller, M., Rodriguez, E., Roth, L., Seal,
562 D., Shaffer, S., Shimada, J., Umland, J., Werner, M., Oskin, M., Burbank, D., and Alsdorf, D.: The Shuttle Radar Topography
563 Mission, *Rev. Geophys.*, 45, RG2004, doi: 10.1029/2005RG000183, 2007.



- 564 Faroux, S., Kaptué Tchuenté, A. T., Roujean, J.-L., Masson, V., Martin, E., and Le Moigne, P.: ECOCLIMAP-II/Europe: a
565 twofold database of ecosystems and surface parameters at 1 km resolution based on satellite information for use in land surface,
566 meteorological and climate models, *Geosci. Model Dev.*, 6, 563-582, doi: 10.5194/gmd-6-563-2013, 2013.
- 567 Gascoïn, S., Ducharne, A., Ribstein, P., Perroy, E., and Wagnon, P.: Sensitivity of bare soil albedo to surface soil moisture on
568 the moraine of the Zongo Glacier (Bolivia), *Geophys. Res. Lett.*, 36, L02405, doi: 10.1029/2008GL036333, 2009.
- 569 Goodwell, A., Zahan, M., Cao, J. Z., and Urycki, D. R.: Spatial heterogeneity of agricultural evapotranspiration as quantified
570 by satellite and flux tower sources, *Agric. For. Meteorol.*, 372, 110608, doi: 10.1016/j.agrformet.2024.110608, 2025.
- 571 Han, Q., Zeng, Y. J., Zhang, L. J., Wang, C., Prikaziuk, E., Niu, Z. G., and Su, B.: Global long-term daily 1 km surface soil
572 moisture dataset with physics-informed machine learning, *Sci. Data*, 10, 101, doi: 10.1038/s41597-023-02071-0, 2023.
- 573 Han, Q., Zeng, Y. J., Zhang, L. J., Wang, C., Prikaziuk, E., Niu, Z. G., and Su, B.: Global long-term daily 1 km surface soil
574 moisture dataset with physics-informed machine learning (GSSM1 km), figshare [data set], doi:
575 10.6084/m9.figshare.21806457.v2, 2022.
- 576 Hapke, B.: Bidirectional reflectance spectroscopy: 1. Theory, *J. Geophys. Res. Solid Earth*, 86, 3039-3054, doi:
577 10.1029/JB086iB04p03039, 1981.
- 578 Härer, S., Bernhardt, M., Siebers, M., and Schulz, K.: On the need for a time- and location-dependent estimation of the NDSI
579 threshold value for reducing existing uncertainties in snow cover maps at different scales, *The Cryosphere*, 12, 1629-1642,
580 doi: 10.5194/tc-12-1629-2018, 2018.
- 581 He, T., Gao, F., Liang, S., and Peng, Y.: Mapping climatological bare soil albedos over the contiguous United States using
582 MODIS data, *Remote Sens.*, 11, 666, doi: 10.3390/rs11060666, 2019.
- 583 Hengl, T., Wheeler, I.: Soil organic carbon content in $\times 5 \text{ g kg}^{-1}$ at 6 standard depths (0, 10, 30, 60, 100, and 200 cm) at 250
584 m resolution (Version v02) [data set], doi: 10.5281/zenodo.2525664, 2018.
- 585 Hengl, T.: Sand content in % (kg kg^{-1}) at 6 standard depths (0, 10, 30, 60, 100, and 200 cm) at 250 m resolution (Version v02)
586 [data set], doi: 10.5281/zenodo.2525667, 2018.
- 587 Hengl, T.: Soil bulk density (fine earth) $\times 10 \text{ kg m}^{-3}$ at 6 standard depths (0, 10, 30, 60, 100, and 200 cm) at 250 m resolution
588 (Version v02) [data set], doi: 10.5281/zenodo.2525665, 2018.
- 589 Hengl, T.: Soil pH in H_2O at 6 standard depths (0, 10, 30, 60, 100, and 200 cm) at 250 m resolution (Version v02) [data set],
590 doi: 10.5281/zenodo.2525666, 2018.
- 591 Hersbach, H., Bell, B., Berrisford, P., et al.: The ERA5 global reanalysis, *Q. J. R. Meteorol. Soc.*, 146, 1999-2049, doi:
592 10.1002/qj.3803, 2020.
- 593 Harmel, T., Chami, M., Tormos, T., Reynaud, N., and Danis, P. A.: Sunlint correction of the Multi-Spectral Instrument (MSI)-
594 Sentinel-2 imagery over inland and sea waters from SWIR bands, *Remote Sens. Environ.*, 204, 308-321, doi:
595 10.1016/j.rse.2017.10.044, 2018.
- 596 Heuscher, S. A., Brandt, C. C., and Jardine, P. M.: Using soil physical and chemical properties to estimate bulk density, *Soil
597 Sci. Soc. Am. J.*, 69, 51-56, doi: 10.2136/sssaj2005.0051, 2005.



- 598 Houldcroft, C. J., Grey, W. M. F., Barnsley, M., Taylor, C. M., Los, S. O., and North, P. R. J.: New vegetation albedo
599 parameters and global fields of soil background albedo derived from MODIS for use in a climate model, *J. Hydrometeorol.*,
600 10, 183-198, doi: 10.1175/2008JHM1055.1, 2009.
- 601 Idso, S. B., Jackson, R. D., Reginato, R. J., Kimball, B. A., and Nakayama, F. S.: The dependence of bare soil albedo on soil
602 water content, *J. Appl. Meteorol. Climatol.*, 14, 109-113, doi: 10.1175/1520-0450(1975)014<0109:TDOBSA>2.0.CO;2, 1975.
- 603 Jr, C. T. G., Kang, S. H., Brice, D. J., and Schadt, C. W.: Variability in soil properties at different spatial scales (1 m-1 km) in
604 a deciduous forest system, *Soil Biol. Biochem.*, 39, 2621-2627, doi: 10.1016/j.soilbio.2007.05.019, 2007.
- 605 Jacquemoud, S., Baret, F., and Hanocq, J. F.: Modeling spectral and bidirectional soil reflectance, *Remote Sens. Environ.*, 41,
606 123-132, doi: 10.1016/0034-4257(92)90028-J, 1992.
- 607 Jones, N.: How machine learning could help to improve climate forecasts, *Nature*, 548, 379, doi: 10.1038/548379a, 2017.
- 608 Korchagina, I. A., Goleva, O. G., Savchenko, Y. Y., and Bozhikov, T. S.: The use of geographic information systems for forest
609 monitoring, *J. Phys. Conf. Ser.*, 1515, 032077, doi: 10.1088/1742-6596/1515/3/032077, 2020.
- 610 Lesaignoux, A., Fabre, S., Briottet, X., and Olioso, A.: Soil moisture impact on lab measured reflectance of bare soils in the
611 optical domain [0.4–15 μm], 2009 IEEE Int. Geosci. Remote Sens. Symp., Cape Town, South Africa, III-522-III-525, doi:
612 10.1109/IGARSS.2009.5417807, 2009.
- 613 Lin, X., Wu, S., Chen, B., Lin, Z., Yan, Z., Chen, X., Yin, G., You, D., Wen, J., Liu, Q., Xiao, Q., Liu, Q., and Laforteza, R.:
614 Estimating 10-m land surface albedo from Sentinel-2 satellite observations using a direct estimation approach with Google
615 Earth Engine, *ISPRS J. Photogramm. Remote Sens.*, 194, 1-20, doi: 10.1016/j.isprsjprs.2022.10.001, 2022.
- 616 Liu, W., Baret, F., Gu, X., Tong, Q., Zheng, L., and Zhang, B.: Relating soil surface moisture to reflectance, *Remote Sens.*
617 *Environ.*, 81, 238-246, doi: 10.1016/S0034-4257(02)00062-2, 2002.
- 618 Liu, J., Schaaf, C., Strahler, A., Jiao, Z., Shuai, Y., Zhang, Q., Roman, M., Augustine, J. A., and Dutton, E. G.: Validation of
619 Moderate Resolution Imaging Spectroradiometer (MODIS) albedo retrieval algorithm: dependence of albedo on solar zenith
620 angle, *J. Geophys. Res.*, 114, D09103, doi: 10.1029/2008JD010522, 2009.
- 621 Masson, V., Champeaux, J.-L., Chauvin, F., Meriguet, C., and Lacaze, R.: A global database of land surface parameters at 1-
622 km resolution in meteorological and climate models, *J. Climate*, 16, 1261-1282, doi: 10.1175/1520-
623 0442(2003)016<1261:AGDOLS>2.0.CO;2, 2003.
- 624 Matthias, A. D., Fimbres, A., Sano, E. E., Post, D. F., Accioly, L., Batchily, A. K., and Ferreira, L. G.: Surface roughness
625 effects on soil albedo, *Soil Sci. Soc. Am. J.*, 64, 1035-1041, doi: 10.2136/sssaj2000.6441035x, 2000.
- 626 Mohr, J., Tewes, A., Ahrends, H., and Gaiser, T.: Assessing the within-field heterogeneity using RapidEye NDVI time series
627 data, *Agriculture*, 13, 1029, doi: 10.3390/agriculture13101029, 2023.
- 628 Nguyen, T. T.: Predicting agricultural soil carbon using machine learning, *Nat. Rev. Earth Environ.*, 2, 825, doi:
629 10.1038/s43017-021-00219-4, 2021.
- 630 USDA NRCS: Web Soil Survey, available online: <http://websoilsurvey.sc.egov.usda.gov/>, accessed 20 November 2023.



- 631 Pastorello, G., Trotta, C., Canfora, E. et al.: The FLUXNET2015 dataset and the ONEFlux processing pipeline for eddy
632 covariance data, *Sci. Data*, 7, 225, doi: 10.1038/s41597-020-00787-8, 2020.
- 633 Pan, F., Wu, X., Zeng, Q., Tang, R., Wang, J., Lin, X., You, D., Wen, J., and Xiao, Q.: A coarse pixel-scale ground “truth”
634 dataset based on global in situ site measurements to support validation and bias correction of satellite surface albedo products,
635 *Earth Syst. Sci. Data*, 16, 161–176, doi: 10.5194/essd-16-161-2024, 2024.
- 636 Pinty, B., Andredakis, I., Clerici, M., Kaminski, T., Taberner, M., Verstraete, M. M., Gobron, N., Plummer, S., and Widlowski,
637 J.-L.: Exploiting the MODIS albedos with the Two-stream Inversion Package (JRC-TIP): 1. Effective leaf area index,
638 vegetation, and soil properties, *J. Geophys. Res.*, 116, D09105, doi: 10.1029/2010JD015372, 2011.
- 639 Post, D. F., Fimbres, A., Matthias, A. D., Sano, E. E., Accioly, L., Batchily, A. K., and Ferreira, L. G.: Predicting soil albedo
640 from soil color and spectral reflectance data, *Soil Sci. Soc. Am. J.*, 64, 1027-1034, doi: 10.2136/sssaj2000.6441027x, 2000.
- 641 Praeg, N.: The role of land management and elevation in shaping soil microbial communities: insights from the Central
642 European Alps, *Soil Biol. Biochem.*, 150, 107951, doi: 10.1016/j.soilbio.2020.107951, 2020.
- 643 Qiu, S., Zhu, Z., and He, B.: Fmask 4.0: Improved cloud and cloud shadow detection in Landsats 4-8 and Sentinel-2 imagery,
644 *Remote Sens. Environ.*, 231, 111205, doi: 10.1016/j.rse.2019.111205, 2019.
- 645 Rizzo, R., Wadoux, A. M. J.-C., Demattê, J. A. M., Minasny, B., Barrón, V., Ben-Dor, E., Francos, N., Savin, I., Poppiel, R.,
646 Silvero, N. E. Q., Terra, F. da S., Rosin, N. A., Rosas, J. T. F., Greschuk, L. T., Ballester, M. V. R., Rico Gómez, A. M.,
647 Bellinaso, H., Safanelli, J. L., Chabrilat, S., Fiorio, P. R., and Salama, E. S. M.: Remote sensing of the Earth's soil color in
648 space and time, *Remote Sens. Environ.*, 299, 113845, doi: 10.1016/j.rse.2023.113845, 2023.
- 649 Roujean, J.-L., Leon-Tavares, J., Smets, B., Claes, P., Camacho De Coca, F., and Sanchez-Zapero, J.: Surface albedo and
650 TOC-R 300 m products from PROBA-V instrument in the framework of Copernicus Global Land Service, *Remote Sens.*
651 *Environ.*, 215, 57–73, doi: 10.1016/j.rse.2018.05.031, 2018.
- 652 Riggs, G. A., Hall, D. K., and Román, M. O.: MODIS snow products user guide for collection 6, NSIDC – US National Snow
653 and Ice Data Center, Boulder, CO, <http://modis-snow-ice.gsfc.nasa.gov/?c=userguide>, last access: 13 April 2022, 2016.
- 654 Ren, H., Cromwell, E., Kravitz, B., and Chen, X.: Technical note: using long short-term memory models to fill data gaps in
655 hydrological monitoring networks, *Hydrol. Earth Syst. Sci.*, 26, 1727-1743, doi: 10.5194/hess-26-1727-2022, 2022.
- 656 Roosjen, P. P. J., Bartholomeus, H. M., and Clevers, J. G. P. W.: Effects of soil moisture content on reflectance anisotropy-
657 laboratory goniometer measurements and RPV model inversions, *Remote Sens. Environ.*, 170, 229-238, doi:
658 10.1016/j.rse.2015.08.015, 2015.
- 659 Reichstein, M., Camps-Valls, G., Stevens, B., Jung, M., Denzler, J., Carvalhais, N and Prabhat: Deep learning and process
660 understanding for data-driven Earth system science. *Nature* 566, 195-204, doi: 10.1038/s41586-019-0912-1, 2019.
- 661 Sadeghi, M., Babaeian, E., Tuller, M., and Jones, S. B.: Particle size effects on soil reflectance explained by an analytical
662 radiative transfer model, *Remote Sens. Environ.*, 210, 375-386, doi: 10.1016/j.rse.2018.03.028, 2018.
- 663 Sieber, P., Böhme, S., Ericsson, N., and Hansson, P. A.: Albedo on cropland: field-scale effects of current agricultural practices
664 in Northern Europe, *Agric. For. Meteorol.*, 321, 108978, doi: 10.1016/j.agrformet.2022.108978, 2022.



- 665 Starr, J., Zhang, J., Reid, J. S., and Roberts, D. C.: Albedo impacts of changing agricultural practices in the United States
666 through space-borne analysis, *Remote Sens.*, 12, 2887, doi: 10.3390/rs12172887, 2020.
- 667 Sugathan, N., Biju, V., and Renuka, G.: Influence of soil moisture content on surface albedo and soil thermal parameters at a
668 tropical station, *J. Earth Syst. Sci.*, 123, 1115-1128, doi: 10.1007/s12040-014-0456-7, 2014.
- 669 Sun, Z., Lv, Y., and Lu, S.: An assessment of the bidirectional reflectance models basing on laboratory experiment of natural
670 particulate surfaces, *J. Quant. Spectrosc. Radiat. Transf.*, 163, 102-119, doi: 10.1016/j.jqsrt.2015.01.004, 2015.
- 671 Sudmanns, M., Tiede, D., Augustin, H., and Lang, S.: Assessing global Sentinel-2 coverage dynamics and data availability for
672 operational Earth observation (EO) applications using the EO-Compass, *Int. J. Digit. Earth*, 13, 768-784, doi:
673 10.1080/17538947.2019.1583143, 2019.
- 674 Sirisathitkul, Y., and Sirisathitkul, C.: Decoding soil color: origins, influences, and methods of analysis, *AgriEngineering*, 7,
675 58, doi: 10.3390/agriengineering7030058, 2025.
- 676 Szabó, B., Kassai, P., Plunge, S., Nemes, A., Braun, P., Strauch, M., Witing, F., Mészáros, J., and Čerkasova, N.: Addressing
677 soil data needs and data-gaps in catchment scale environmental modeling: the European perspective, *EGUsphere*, 10, 587-617,
678 doi: 10.5194/egusphere-10-587-2024, 2024.
- 679 Verheijen, F. G. A., Jeffery, S., Velde, M. V. D., and Penizek, V.: Reductions in soil surface albedo as a function of biochar
680 application rate: implications for global radiative forcing, *Environ. Res. Lett.*, 8, 044008, doi: 10.1088/1748-9326/8/4/044008,
681 2013.
- 682 Wang, X., Chen, S., Zhou, C., Duan, S. B., and Shi, Z.: Cross-sensor data reconstruction for optical remote sensing gap-filling
683 with attention-enhanced multi-scale fusion network, *Int. J. Appl. Earth Obs. Geoinf.*, 140, 104571, doi:
684 10.1016/j.jag.2025.104571, 2025.
- 685 Wen, J. G., Zhao, X. J., Liu, Q., Tang, Y., and Dou, B. C.: An improved land-surface albedo algorithm with DEM in rugged
686 terrain, *IEEE Geosci. Remote Sens. Lett.*, 11, 883-887, doi: 10.1109/LGRS.2013.2245652, 2013.
- 687 Yang, F., Mitchell, K., Hou, Y.-T., Dai, Y., Zeng, X., Wang, Z., and Liang, X.-Z.: Dependence of land surface albedo on solar
688 zenith angle: observations and model parameterization, *J. Appl. Meteorol. Climatol.*, 47, 2963-2982, doi:
689 10.1175/2008JAMC1843.1, 2008.
- 690 Yang, X., Li, J., Yu, Q., Ma, Y., Tong, X., Feng, Y., and Tong, Y.: Impacts of diffuse radiation fraction on light use efficiency
691 and gross primary production of winter wheat in the North China Plain, *Agric. For. Meteorol.*, 275, 233-242, doi:
692 10.1016/j.agrformet.2019.05.028, 2019.
- 693 Yu, K., Su, Y., Ciaia, P., Lauerwald, R., Ceschia, E., Makowski, D., Xu, Y., Abbessi, E., Bazzi, H., Tallec, T., Brut, A.,
694 Heinesch, B., Brümmer, C., Schmidt, M., Acosta, M., Buysse, P., Gruenwald, T., and Goll, D. S.: Quantifying albedo impact
695 and radiative forcing of management practices in European wheat cropping systems, *Environ. Res. Lett.*, 19, 074042, doi:
696 10.1088/1748-9326/ad5859, 2024.



- 697 Yu, K., Su, Y., Ciais, P., Lauerwald, R., Makowski, D., Shi, T. Q., Wu, S. B., Sieber, P., Zhou, C. L., and Goll, D.: Bare soil
698 albedo datasets at high spatio-temporal resolution from Sentinel-2 observations. figshare. Dataset. doi:
699 [10.6084/m9.figshare.30488027.v1](https://doi.org/10.6084/m9.figshare.30488027.v1), 2025.
- 700 Yue, J. B., and Tian, Q. J.: Estimating fractional cover of crop, crop residue, and soil in cropland using broadband remote
701 sensing data and machine learning, *Int. J. Appl. Earth Obs. Geoinf.*, 89, 102089, doi: 10.1016/j.jag.2020.102089, 2020.
- 702 Zanaga, D., Van De Kerchove, R., Daems, D., De Keersmaecker, W., Brockmann, C., Kirches, G., Wevers, J., Cartus, O.,
703 Santoro, M., Fritz, S., Lesiv, M., Herold, M., Tsendbazar, N. E., Xu, P., Ramoino, F., and Arino, O.: ESA WorldCover 10 m
704 2021 v200, doi: 10.5281/zenodo.7254221, 2022.
- 705 Zhang, X., Jiao, Z., Zhao, C., Qu, Y., Liu, Q., Zhang, H., Tong, Y., Wang, C., Li, S., Guo, J., Zhu, Z., Yin, S., & Cui, L.:
706 Review of Land Surface Albedo: Variance Characteristics, Climate Effect and Management Strategy. *Remote Sens.*, 14(6),
707 1382. doi: 10.3390/rs14061382, 2022.
- 708 Zhang, Y., Narayanappa, D., Ciais, P., Li, W., Goll, D., Vuichard, N., De Kauwe, M. G., Li, L., and Maignan, F.: Evaluating
709 the vegetation-atmosphere coupling strength of ORCHIDEE land surface model (v7266), *Geosci. Model Dev.*, 15, 9111–9125,
710 doi: 10.5194/gmd-15-9111-2022, 2022.
- 711 Zhou, L., Dickinson, R. E., and Tian, Y.: Derivation of a soil albedo dataset from MODIS using principal component analysis:
712 Northern Africa and the Arabian Peninsula, *Geophys. Res. Lett.*, 32, L21407, doi: 10.1029/2005GL024448, 2005.